

See discussions, stats, and author profiles for this publication at: <https://www.researchgate.net/publication/240475499>

Spin Crossover Phenomenon in Nanocrystals and Nanoparticles of $[\text{Fe}(\text{3-Fpy})_2\text{M}(\text{CN})_4]$ ($\text{M}^{\text{II}} = \text{Ni}, \text{Pd}, \text{Pt}$) Two-Dimensional Coordination Polymers

ARTICLE *in* CHEMISTRY OF MATERIALS · JULY 2010

Impact Factor: 8.35 · DOI: 10.1021/cm101022u

CITATIONS

59

READS

61

7 AUTHORS, INCLUDING:



Ashis Bhattacharjee

Visva Bharati University

95 PUBLICATIONS 981 CITATIONS

SEE PROFILE

Spin Crossover Phenomenon in Nanocrystals and Nanoparticles of [Fe(3-Fpy)₂M(CN)₄] (M^{II} = Ni, Pd, Pt) Two-Dimensional Coordination Polymers

Victor Martínez,^{†,§} Ishtvan Boldog,[†] Ana Belén Gaspar,^{*,†} Vadim Ksenofontov,[‡]
Ashis Bhattacharjee,[‡] Philipp Gütllich,[‡] and José Antonio Real^{*,†}

[†]Institut de Ciència Molecular/Departament de Química Inorgànica, Universitat de València, Edifici de
Instituts de Paterna, Apartat de Correus 22085, 46071 València, Spain, and [‡]Institut für Anorganische und
Analytische Chemie, Johannes-Gutenberg-Universität, Staudinger-Weg 9, D-55099 Mainz, Germany.

[§]Present address: Departamento de Química, Facultad de Ciencias, Universidad de Los Andes, Carrera 1 No.
18A - 10/70, Bogotá, Colombia.

Received April 13, 2010. Revised Manuscript Received June 10, 2010

The two-dimensional spin crossover (SCO) polymers [Fe(3-Fpy)₂M(CN)₄] (M^{II} = Ni(**1**), Pd(**2**), Pt(**3**)) were nanostructured in the form of nanocrystals and nanoparticles, and their chemical, structural, and physical characterization was carried out using different experimental methods (powder X-ray diffraction, magnetic susceptibility measurements, Mössbauer and infrared spectroscopy, transmission and scanning electronic microscopy, etc.). Surfactant-free nanocrystals of average dimensions 400 × 400 × 30 nm (**1a**, **1a**^{*}, **2a**, **3a**) were synthesized from water in oil microemulsions (w/o) while nanoparticles of average size 200 × 100, 100 × 60, and 70 × 30 nm were obtained in poly(vinylpyrrolidone) (PVP) coating polymer (**1b**–**1d**, **2b**, **2b**^{*}, and **3b**). The spin crossover process is drastically influenced by the dimensions of the crystal/particle. Nanocrystals of **1**–**3** exhibit a quasi complete first-order spin transition centered within the interval 200–225 K, while PVP-coated nanoparticles undergo continuous second order spin transition at much lower temperatures (ca. 160 K).

Introduction

Special attention is currently given to iron(II) spin crossover (SCO) compounds exhibiting cooperative behavior

since they can manifest sensory and memory functions.¹ SCO compounds represent a type of functional molecular material possessing labile electronic configurations switchable between the high- (HS) and low-spin (LS) states in response to external stimuli (temperature,^{1a–c,2} pressure,^{1a–c,2} light,^{1a,e,3} or guest absorption/desorption^{1f–i}). In the HS and LS states they manifest differences in magnetism, optical properties, dielectric constant, color, and structure.

A rational control of the growth of these materials at the nanometric scale and the study of the size-dependent SCO properties is crucial for their successful integration in functional devices.^{4–14} In fact, determining the critical particle size or film thickness which preserves a complete spin transition with hysteretic behavior is an essential aspect in the nanominiaturization of a SCO material.

*To whom correspondence should be addressed. E-mail: ana.b.gaspar@uv.es (A.B.G.), jose.a.real@uv.es (J.A.R.).

- (1) (a) Gütllich, P.; Goodwin, H. A., Eds.; *Spin Crossover in Transition Metal Compounds. Topics in Current Chemistry*; Springer Verlag: Berlin, 2004; Vols. 233, 234, 235. (b) Gaspar, A. B.; Ksenofontov, V.; Seredyuk, M.; Gütllich, P. *Coord. Chem. Rev.* **2005**, *249*, 2661. (c) Real, J. A.; Gaspar, A. B.; Muñoz, M. C. *Dalton Trans.* **2005**, 2062. (d) Real, J. A.; Gaspar, A. B.; Niel, V.; Muñoz, M. C. *Coord. Chem. Rev.* **2003**, *236*, 121. (e) Gütllich, P.; Hauser, A.; Spiering, H. *Angew. Chem., Int. Ed. Engl.* **1994**, *33*, 2024. (f) Ohba, M.; Yoneda, K.; Agustí, G.; Muñoz, M. C.; Gaspar, A. B.; Real, J. A.; Yamasaki, M.; Ando, H.; Nakao, Y.; Sakaki, S.; Kitagawa, S. *Angew. Chem., Int. Ed.* **2009**, *48*, 4767. (g) Real, J. A.; Andrés, E.; Muñoz, M. C.; Julve, M.; Granier, T.; Bousseksou, A.; Varret, F. *Science* **1995**, *268*, 265–267. (h) Halder, G. J.; Kepert, C. J.; Moubarak, B.; Murray, K. S.; Cashion, J. D. *Science* **2002**, *298*, 1762–1765. (i) Neville, S. M.; Halder, G. J.; Chapman, K. W.; Duriska, M. B.; Southon, P. D.; Cashion, J. D.; Létard, J. F.; Moubarak, B.; Murray, K. S.; Kepert, C. J. *J. Am. Chem. Soc.* **2008**, *130*, 2869–2876.
- (2) (a) Galet, A.; Gaspar, A. B.; Muñoz, M. C.; Bukin, G. V.; Levchenko, G.; Real, J. A. *Adv. Mater.* **2005**, *17*, 2949. (b) Kahn, O.; Martínez, C. J. *Science* **1998**, *279*, 44. (c) Kahn, O.; Kröber, J.; Jay, C. *Adv. Mater.* **1992**, *4*, 718.
- (3) (a) Ould Moussa, N.; Molnár, G.; Bonhommeau, S.; Zwick, A.; Mouri, S.; Tanaka, K.; Real, J. A.; Bousseksou, A. *Phys. Rev. Lett.* **2005**, *94*, 107205. (b) Ould Moussa, N.; Trzop, E.; Mouri, S.; Zein, S.; Molnár, G.; Gaspar, A. B.; Collet, E.; Buron, M.; Real, J. A.; Borshch, S.; Tanaka, K.; Cailleau, H.; Bousseksou, A. *Phys. Rev. B* **2007**, *75*, 054101. (c) Trzop, E.; Buron-Le Cointe, M.; Calleau, H.; Toupet, L.; Molnár, G.; Bousseksou, A.; Gaspar, A. B.; Real, J. A.; Collet, E. *J. Appl. Crystallogr.* **2007**, *40*, 158. (d) Bonhommeau, S.; Molnár, G.; Galet, A.; Zwick, A.; Real, J. A.; McGarvey, J. J.; Bousseksou, A. *Angew. Chem., Int. Ed.* **2005**, *44*, 4069.

- (4) (a) Ozin, G. A.; Arsenault, A. C. *Nanochemistry: A Chemical Approach to Nanomaterials*, The Royal Society of Chemistry: Cambridge, 2005, ISBN 0-85404-664-X. (b) Burda, C.; Chen, X.; Narayanan, R.; El-Sayed, M. A. *Chem. Rev.* **2005**, *105*, 1025.
- (5) (a) Hollingsworth, M. D. *Science* **2002**, *295*, 2410. (b) Janiak, C. *J. Chem. Soc., Dalton Trans.* **2003**, 2781. (c) Kitagawa, S.; Kitaura, R.; Noro, S. *Angew. Chem., Int. Ed.* **2004**, *43*, 2334. (d) Maspoch, D.; Ruiz-Molina, D.; Veciana, J. *Chem. Soc. Rev.* **2007**, *36*, 770.
- (6) (a) Vaucher, S.; Li, M.; Mann, S. *Angew. Chem., Int. Ed.* **2000**, *39*, 1793. (b) Vaucher, S.; Fielden, J.; Li, M.; Dujardin, E.; Mann, S. *Nano Lett.* **2002**, *2*, 225. (c) Uemura, T.; Kitagawa, S. *J. Am. Chem. Soc.* **2003**, *125*, 7814. (d) Domínguez-Vera, J. M.; Colacio, E. *Inorg. Chem.* **2003**, *42*, 6983. (e) Catala, L.; Gacoin, T.; Boilot, J. P.; Rivière, E.; Paulsen, C.; Lhotel, E.; Mallah, T. *Adv. Mater.* **2003**, *15*, 826. (f) Moore, J. G.; Lochner, E. J.; Ramsey, C.; Dalal, N. S.; Stiegman, A. E. *Angew. Chem., Int. Ed.* **2003**, *42*, 2741.

In this regard, recent investigations have led to the preparation of nanocrystals^{9,10} and thin films^{11a,b} of the three-dimensional (3D) spin crossover coordination polymer [Fe(pz)Pt(CN)₄]¹⁵ displaying size-dependent spin transition characteristics. Bulk microcrystalline samples of this polymer undergo very cooperative spin transition with cooling and heating critical temperatures at $T_c^{\downarrow} = 285$ K and $T_c^{\uparrow} = 309$ K, respectively. The corresponding nanocrystals of average dimensions $200 \times 200 \times 60$ nm and $60 \times 60 \times 30$ nm display practically complete spin transitions, demonstrating a decrease of critical temperatures and hysteresis width as the crystallites' size diminishes.⁹ This effect is even more marked for 10–20 nm sized nanoparticles, where only around 1/3 of the Fe(II) ions undergo a spin transition characterized by a very narrow thermal hysteresis loop.¹⁰ A similar situation was found for [Fe(pz)Ni(CN)₄] nanoparticles of about 4 nm coated with Chitosan polymer.¹²

A different behavior was observed for surfactant-coated nanoparticles of the triazole-based one-dimensional (1D) spin crossover polymers [Fe(Htrz)₂(trz)](BF₄) (Htrz = 1,2,4-*H*-triazole) and [Fe(4-NH₂trz)₃](Br)₂ (4-NH₂trz = 4-amino-1,2,4-triazole). Twenty nanometer size nanoparticles of the former display a strong cooperative spin transition with a large hysteresis loop just like the one observed for the bulk material¹³ while, in the latter, the abruptness of the spin transition and the hysteresis width diminishes as the particle size decreases with minimal displacement of T_c^{\downarrow} .¹⁴ Nanometric particles of [Fe(4-NH₂trz)₃](Br)₂ are the only example so far investigated

that follow the behavior predicted by Monte Carlo simulations for cubic or spherical spin crossover nanoparticles.¹⁶

To the best of our knowledge the effect of nanostructuring on the spin crossover properties of a two-dimensional (2D) coordination polymer has not yet been reported. To do so, we focused on the 2D coordination polymers [Fe(3-Fpy)₂M(CN)₄] ($M^{II} = \text{Ni(1), Pd(2), Pt(3)}$, and 3-Fpy = 3-fluoropyridine).¹⁷ Polymers **1–3** undergo a very cooperative first order spin transition in the temperature interval 210–250 K accompanied by a drastic change of color (LS (dark pink) and HS (white)). Here we report the synthesis and characterization of nanocrystals and nanoparticles of the polymers **1–3**. Surfactant-free nanocrystals of average dimensions $400 \times 400 \times 30$ nm (**1a**, **1a***, **2a**, **3a**) were synthesized from water-in-oil microemulsions (w/o) and nanoparticles of 200×100 , 100×60 , and 70×30 nm were prepared using the coating polymer poly(vinylpyrrolidone) (PVP) (**1b–1d**, **2b**, **2b'**, and **3b**). Nanocrystals of **1–3** exhibit quasi complete first-order spin transitions centered in the interval 200–225 K, while PVP coated nanoparticles undergo a continuous second order spin transition at much lower temperatures (ca. 160 K). We shall present an analysis of the modification of the spin transition characteristics in the nanostructured materials as a consequence of the particle size decrease.

Experimental Section

Materials. Fe(BF₄)₂·6H₂O (97%) and 3-fluoropyridine (99%+) were obtained from Sigma-Aldrich, K₂Ni(CN)₄·5H₂O, K₂Pd(CN)₄·3H₂O, and K₂Pt(CN)₄·3H₂O (the water content was derived from titration results given in the certificate) were obtained from Strem and used as received. PVP (technical grade, K-30, MW ~ 40000) was obtained from Fluka. Sodium bis-(2-ethylhexyl) sulfosuccinate NaAOT (96%) and octane (97%) were obtained from Acros and used without further purification. The deionized water used for synthesis was deoxygenated by simultaneous sonication and argon bubbling during 1 h.

Synthesis of 1a–3a and 1a*. Two solutions containing 9.87 g (22.2 mmol) of NaAOT in 44 mL of octane were prepared in 100 mL dry spherical flasks. 33.8 mg (0.1 mmol) of Fe(BF₄)₂·6H₂O and 38.8 mg (0.4 mmol, 2× excess) of 3-fluoropyridine were dissolved in 2 mL of water and stirred for 2 min. The formed solution was transferred dropwise to one of the flasks containing the NaAOT solution and stirred until formation of a light yellow transparent water in oil (w/o) microemulsion. Similarly, a solution of 0.1 mmol of K₂[M^{II}(CN)₄] (24.1 mg Ni, 28.4 mg Pd, 43 mg Pt in 2 mL of water was transferred dropwise to the second NaAOT solution under intensive stirring which resulted in a formation of a slightly opalescent solution, even when taking care of making a very slow addition (approximately 5 min). The obtained w/o solutions ($\omega = [\text{H}_2\text{O}]/[\text{NaAOT}] = 5$, both concentrations related to the total volume of octane) were stirred for ~15 min, then quickly combined in a flask previously purged with argon, and the resulting solution was left under stirring. Signs of precipitation appeared after ~10 min of stirring, and

- (7) (a) Clavel, G.; Guari, Y.; Larionova, J.; Guérin, C. *New J. Chem.* **2005**, 29, 275. (b) Catala, L.; Mathonière, C.; Gloter, A.; Stephan, O.; Gacoin, T.; Boilot, J. P.; Mallah, T. *Chem. Commun.* **2005**, 746. (c) Catala, L.; Gloter, A.; Stephan, O.; Rogez, G.; Mallah, T. *Chem. Commun.* **2006**, 1018. (d) Clavel, G.; Larionova, J.; Guari, Y.; Guérin, C. *Chem.—Eur. J.* **2005**, 12, 3798.
- (8) (a) Imaz, I.; Maspocho, D.; Rodríguez-Blanco, C.; Pérez-Falcón, J. M.; Campo, J.; Ruiz-Molina, D. *Angew. Chem., Int. Ed.* **2008**, 47, 1857–1860. (b) Jung, S.; Oh, M. *Angew. Chem., Int. Ed.* **2008**, 47, 2049.
- (9) Boldog, I.; Gaspar, A. B.; Martínez, V.; Pardo-Ibañez, P.; Ksenofontov, V.; Bhattacharjee, A.; Gülich, P.; Real, J. A. *Angew. Chem., Int. Ed.* **2008**, 47, 6433.
- (10) Volatron, F.; Catala, L.; Riviere, E.; Gloter, A.; Stephan, O.; Mallah, T. *Inorg. Chem.* **2008**, 47, 6584.
- (11) (a) Cobo, S.; Molnar, G.; Real, J. A.; Bousseksou, A. *Angew. Chem., Int. Ed.* **2006**, 45, 5786. (b) Molnar, G.; Cobo, S.; Real, J. A.; Carcenac, F.; Daran, E.; Vieu, C.; Bousseksou, A. *Adv. Mater.* **2007**, 19, 2163. (c) Agustí, G.; Cobo, S.; Gaspar, A. B.; Molnár, G.; Ould Moussa, N.; Szilágyi, P. A.; Pálfi, V.; Vieu, C.; Muñoz, M. C.; Real, J. A.; Bousseksou, A. *Chem. Mater.* **2008**, 20, 6721.
- (12) Larionova, J.; Salmon, L.; Guari, Y.; Tokarev, A.; Molvinger, K.; Molnar, G.; Bousseksou, A. *Angew. Chem., Int. Ed.* **2008**, 47, 8236.
- (13) Coronado, E.; Galán-Mascarós, J. R.; Monrabal-Capilla, M.; García-Martínez, J.; Pardo-Ibañez, P. *Adv. Mater.* **2007**, 19, 1359.
- (14) (a) Létard, J. F.; Nguyen, N.; Daro, N. PCT/FR 2006/002651 (in French), 2007, WO 2007065996, p 31. (b) Forestier, T.; Mornet, S.; Daro, N.; Nishihara, T.; Mouri, S.; Tanaka, K.; Fouché, O.; Freysz, E.; Létard, J. F. *Chem. Commun.* **2008**, 4327. (c) Forestier, T.; Kaiba, A.; Stanislav, P.; Denux, D.; Guionneau, P.; Etrillard, C.; Daro, N.; Freysz, E.; Létard, J. F. *Chem.—Eur. J.* **2009**, 15, 6122.
- (15) (a) Niel, V.; Martínez-Agudo, J. M.; Muñoz, M. C.; Gaspar, A. B.; Real, J. A. *Inorg. Chem.* **2001**, 40, 3838. (b) Tayagaki, T.; Galet, A.; Molnár, G.; Muñoz, M. C.; Zwick, A.; Tanaka, K.; Real, J. A.; Dubrovinsky, L.; Bousseksou, A. *J. Phys. Chem. B* **2005**, 109, 14859. (c) Molnár, G.; Niel, V.; Gaspar, A. B.; Real, J. A.; Zwick, A.; Bousseksou, A.; McGarvey, J. J. *J. Phys. Chem. B* **2005**, 109, 14859.

- (16) Kawamoto, T.; Abe, S. *Chem. Commun.* **2005**, 3933.

- (17) (a) Martínez, V.; Gaspar, A. B.; Muñoz, M. C.; Bukin, G. V.; Levchenko, G.; Real, J. A. *Chem.—Eur. J.* **2009**, 15, 10960. (b) Martínez, V., Ph.D. Thesis, University of Valencia, Valencia, Spain, July 2009.

Table 1. Codes, Composition and Particles Sizes for the Discussed Compounds

compound	average size (nm)	[Fe(3-Fpy) ₂ Ni(CN) ₄]	[Fe(3-Fpy) ₂ Pd(CN) ₄]	[Fe(3-Fpy) ₂ Pt(CN) ₄]
bulk microcrystalline	> 1000	1	2	3
surfactant-free nanocrystals	400 × 400 × 30	1a, 1a*	2a	3a
PVP coated nanoparticles	200 × 120	1b, 1b'	2b, 2b'	3b
PVP coated nanoparticles	170 × 60	1c		
PVP coated nanoparticles	70 × 30	1d		

the reaction was seemingly completed within a few hours. After 2 days of stirring the precipitate was centrifuged out at 3500 rpm during 30 min yielding a slightly yellow precipitate and a slightly colored supernatant. The precipitate was washed via three cycles of redispersing in 96% ethanol with sonication (just a few seconds to avoid deterioration of the nanocrystals) and 15 min centrifugation. The products were dried under air, yielding **1a**, **2a**, and **3a**, respectively. For **1a*** the synthesis was performed in the same manner but at 0 °C (ice/water bath). The yield of the fine precipitate in repeated experiments was 20–24 mg (50–60%) for **1a–3a** and **1a***. Anal. Calcd for C₁₄H₈F₂FeN₆Ni (**1a** and **1a***): C, 40.74; H, 1.95; N, 20.36; Found: **1a** (**1a***) Found. C, 40.66(40.40); H, 1.97(1.95); N, 20.31(20.29); Anal. Calcd for C₁₄H₈F₂FeN₆Pd (**2a**): C, 36.51; H, 1.75; N, 18.25; Found C, 36.47; H, 1.78; N, 18.21. Anal. Calcd for C₁₄H₈F₂FeN₆Pt (**3a**): C, 30.62; H, 1.47; N, 15.30; EDXA (energy-dispersive X-ray microanalysis) found: (50%Fe:50%Ni) **1a** and **1a***, (50% Fe:50%Pd) **2a**, and (50%Fe:50%Pt) **3a**. Powder X-ray diffraction patterns were recorded for compounds **1a–3a** and **1a*** at 293 K and were found to match those corresponding to the bulk compounds **1–3** (see Supporting Information).

Synthesis of 1b, 1b', 1c, 1d, 2b, 2b', and 3b. **1d.** To a solution of Fe(BF)₄·6H₂O (17 mg, 0.05 mmol) and 3-fluoropyridine (194 mg, 2 mmol) in 10 mL of water was added PVP (222 mg, 2 mmol). The resulting slurry was intensively mixed until the formation of a yellowish, slightly opalescent homogeneous solution. Similarly, a second solution containing 17.5 mg (0.053 mmol) of K₂Ni(CN)₄·5H₂O and 222 mg of PVP in 10 mL of water was prepared. After 15 min of stirring, the two solutions were cooled (0–5 °C) in ice/water bath and quickly combined under intensive stirring. The mixture immediately turned deep yellow, and some opalescence developed within a few minutes reaching its maximum visible saturation in a period of about 30 min. After stirring the mixture for one day, 60 mL of acetone were added under vigorous agitation, and the formed precipitate was centrifuged. To the resulting viscous centrifugate ~2 mL of water were added, and the mixture was redispersed and homogenized. Acetone (6 mL) was added, and the formed precipitate was separated by centrifugation. The redispersion/precipitation procedure was repeated once. The slightly yellow product was dried in vacuum over silica to form a transparent yellow film. Yield: 140 mg. IR: only the ν_{CN}, 2160 cm⁻¹, band related to the embedded coordination compound is discernible, otherwise the spectrum is virtually indistinguishable from the spectrum of pure PVP (see Supporting Information). The rest of compounds were synthesized in a similar manner as described for **1d** (the yields, on similar scale basis, were in the range of 120–180 mg; repeated experiments had had somewhat different yields depending on how much “free” PVP was left in the sample). In the Supporting Information an extensive survey about the quantities of the reactants and volumes used is given. Anal. Calcd for C₁₄H₈F₂FeN₆Ni (**1b–1d**): C, 40.74; H, 1.95; N, 20.36; Anal. Calcd for C₁₄H₈F₂FeN₆Pd (**2b**): C, 36.51; H, 1.75; N, 18.25; Anal. Calcd for C₁₄H₈F₂FeN₆Pt (**3b**): C, 30.62; H, 1.47; N, 15.30; The found percentages of C, N, and H for all samples exceed what expected considering only the formula of the coordination polymer

because of the content of PVP. EDXA (energy-dispersive X-ray microanalysis) found: (50%Fe:50%Ni) **1b–1d**, (50% Fe:50%Pd) **2b, 2b'**, and (50%Fe:50%Pt) **3b**. Powder X-ray diffraction patterns were recorded for compounds **1b, 2b**, and **3b** at 293 K and were found to be poorly resolved; however, broad peaks with maxima of intensity at values of 2θ similar to those observed for the bulk compounds can be identified (see Supporting Information).

Physical Characterization. Variable-temperature magnetic susceptibility measurements of all samples (10–30 mg) were recorded at the rate of 2 K/min on a Quantum Design MPMS2 SQUID susceptometer equipped with a 5.5 T magnet, operating at 1 T and in the 1.8–400 K temperature interval. The susceptometer was calibrated with (NH₄)₂Mn(SO₄)₂·12H₂O. Experimental susceptibilities were corrected for diamagnetism of the constituent atoms using Pascal's constants. Mössbauer spectra were recorded in transmission geometry with a ⁵⁷Co/Rh source kept at room temperature and a conventional spectrometer operating in the constant-acceleration mode. The samples were sealed in Plexiglas sample holders and mounted in a nitrogen or helium bath cryostat. The Recoil 1.03a Mössbauer Analysis Software (Dr. E. Lagarec; <http://www.isapps.ca/recoil/>) was used to fit the experimental spectra. Transmission electron microscopy (TEM) analysis was done in a JEOL microscope mod. JEM-1010 (100KV) equipped with a MegaView III camera. The software used for processing of images was “AnalysIS”. Scanning electron microscopy (SEM) was performed on a HITACHI S-4100 microscope. IR spectra were recorded at 293 K in KBr using a Nicolet 5700 FTIR spectrometer. Thermogravimetry Analysis (TGA) measurements were performed on a Mettler Toledo TGA/SDTA 851e, in the 300–700 K temperature range under nitrogen atmosphere with a rate of 10 K/min. Microanalysis was done by using PV 9760 EDXA Microanalysis with a Philips XL 30 ESEM scanning electron microscope. The equipment used for powder X-ray diffraction (PXRD) characterization of compounds was a Seifert XRD 3003 TT diffractometer, with Bragg–Brentano geometry and Cu tube working at 40 kV with Ni filter (0.3 mm primary slit, 0.3 mm secondary slit, 0.2 mm detector slit, and scintillation detector).

Results

The compounds [Fe(3-Fpy)₂M(CN)₄] (M^{II} = Ni(**1**), Pd(**2**), Pt(**3**)) are presented here in the form of nanocrystals and polymer-coated nanoparticles, and their chemical, structural, and physical characterization was carried out using different experimental methods. Nanocrystals of average dimensions 400 × 400 × 30 nm (**1a, 1a***, **2a, 3a**) were synthesized from water-in-oil microemulsions (w/o) and nanoparticles of average sizes 200 × 100 nm, 100 × 60 nm, and 70 × 30 nm (**1b–1d, 2b, 2b', 3b', and 3b**) were prepared using the coating polymer PVP (Table 1).

All these compounds were found to be isostructural.¹⁶ Figure 1 illustrates the structure of these 2D polymers.

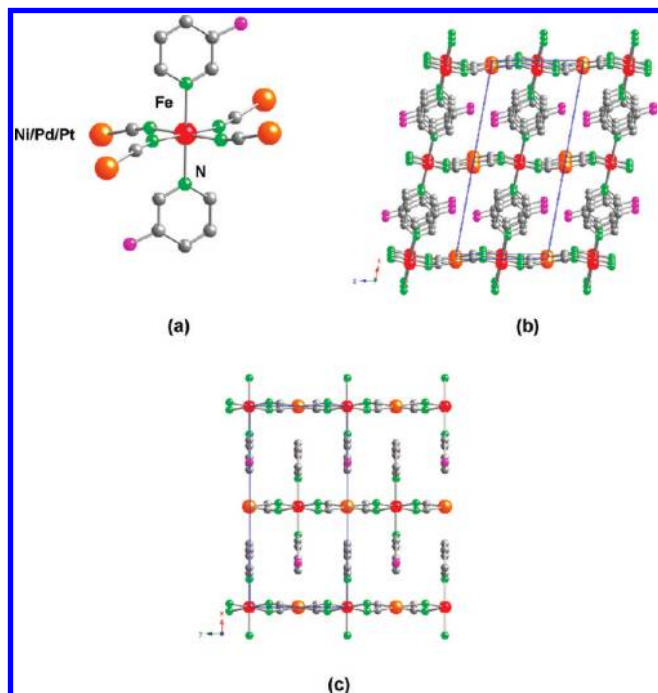


Figure 1. (a) Environment of the Fe(II) SCO center in the $[\text{Fe}(\text{3-Fpy})_2\text{M}(\text{CN})_4]$ ($\text{M}^{\text{II}} = \text{Ni}(\text{I}), \text{Pd}(\text{2}), \text{Pt}(\text{3})$) compounds. (b) View on the 2D layers constituting the structures of **1–3**. (c) Side view on the packing of the 2D layers with interdigitated arrays of axial Fpy ligands of the consecutive layers. Atom code: Fe (red); Ni/Pd/Pt (orange); N (green); C (gray); F (pink).

The iron(II) atom lies at an inversion center which defines an elongated $[\text{FeN}_6]$ pseudooctahedral coordination site (Figure 1a). The equatorial positions are occupied by the nitrogen atoms of four $[\text{M}(\text{CN})_4]^{2-}$ groups. The $\text{Fe}-\text{N}_{\text{eq}}$ bond distances are shorter than the axial positions, which are occupied by the nitrogen atoms of the 3-Fpy ligands. The four equatorial $[\text{M}(\text{CN})_4]^{2-}$ groups are not coplanar with respect to the equatorial plane of the $[\text{FeN}_6]$ octahedron, and each one connects four iron(II) atoms generating an infinite layer (Figure 1b). The layers stack in such a way that the metal atoms of a layer project on the center of the windows defined by the adjacent layers (Figure 1c).

Choice of the Experimental Conditions for Nanocrystal and Nanoparticle Growth and Their Optimization. Nanocrystals of compounds **1–3** were obtained applying the reverse micelle method.¹⁷ The syntheses were performed at room temperature by mixing NaAOT stabilized water-in-oil (w/o) microemulsions containing $\text{Fe}(\text{BF}_4)_2$, 3-Fluoropyridine (3-Fpy) and $\text{K}_2\text{M}(\text{CN})_4$ ($\text{M}^{\text{II}} = \text{Ni}, \text{Pd}, \text{Pt}$) at constant $\omega = [\text{H}_2\text{O}]/[\text{NaAOT}]$ ratio. In a few minutes after mixing of the solutions a distinctive color change from light yellow to intense yellow was observed together with the formation of a fine precipitate of coagulated nanocrystals. Apparently, like for polymer $[\text{Fe}(\text{pz})\text{Pt}(\text{CN})_4]$,⁹ the growth of the nanocrystals takes place via content exchange between microdroplets of the microemulsion, and their precipitation occurs at some particle size threshold apparently because of destabilization of the micelle.¹⁸

A first experiment was performed at $\omega = 5$ with $[\text{Fe}^{\text{II}}] = [\text{Ni}(\text{CN})_4]^{2-} = 0.05 \text{ M}$ and yielded after workup a slightly yellow solid of **1a**. Reproducibility of the synthesis was proven several times (see Supporting Information). Sample **1a** was characterized by TEM (vide infra) and found to be composed by square-shaped nanocrystals of average dimensions $444 \times 444 \times 45 \text{ nm}$. Subsequent syntheses were done by varying ω and the concentration around this initial condition with the purpose of achieving different nanocrystal size (see Supporting Information, Table S1). In general, these syntheses did not afford nanocrystals of better quality than **1a**, excepting the synthesis performed at 0°C . In this case, the nanocrystals isolated, **1a***, exhibit narrower size distribution in comparison with **1a**.

Compound **2a** was obtained using the same ω and $[\text{Fe}^{\text{II}}]$ values as in the synthesis of **1a**, while **3a** was obtained at $[\text{Fe}^{\text{II}}] = 0.025 \text{ M}$. TEM characterization evidenced that **2a** and **3a** show similar square-shaped morphology and dimensions as **1a**.

For the 2D coordination polymers under study no clear correlation between ω , concentration of reactants and particle size was found. Moreover, the formation of nanocrystals is not guaranteed for certain intervals of ω values and concentrations. This situation is in contrast with that previously reported for the 3D SCO coordination polymer $[\text{Fe}(\text{pz})\text{Pt}(\text{CN})_4]$.⁹ In the last case, nanocrystal size decreases as the concentration of the reactants increases in the aqueous phase when $\omega = 5, 10$, or 15 . The growth of the nanocrystal can be controlled in this interval of ω , reaching the micrometer scale at $\omega = 15$.

Given that the attempts to achieve nanocrystals below $400 \times 400 \times 30 \text{ nm}$ using the reverse micelle method were unsuccessful, we decided to explore the formation of nanoparticles/nanocrystals using PVP as a protecting polymer. This method has been applied successfully in the preparation of nanoparticles/nanocrystals of Prussian-blue analogues of average size 16 nm .^{6a–c}

Taking into account the number of key independent parameters in the synthesis ($[\text{PVP}]/[\text{Fe}^{\text{II}}]$ ratio, $[\text{Fe}^{\text{II}}]$, $[\text{3-Fpy}]$, $[\text{M}(\text{CN})_4]^{2-}$, volume and temperature), it is clearly difficult to make a full scan of them. The initial parameters were set by one successful experiment that corresponds to nanoparticles **1d** where $[\text{PVP}]/[\text{Fe}^{\text{II}}] = 40$, $[\text{Fe}^{\text{II}}] = [\text{Ni}(\text{CN})_4]^{2-} = 5 \text{ mM}$, $[\text{3-Fpy}] = 200 \text{ mM}$, $V = 10 \text{ mL}$ and $T = 0^\circ\text{C}$. TEM characterization pointed out an average size of $70 \times 30 \text{ nm}$ for **1d**. Subsequent experiments were performed for changing the conditions around these initially found parameters trying to reach optima for size and quality of the particles. Supporting Information, Table S1 contains the detailed information regarding the $[\text{PVP}]/[\text{Fe}^{\text{II}}]$ ratio, concentrations and volume employed in the different syntheses leading to compounds **1b**, **1b'**, **1c**, **1d**, **2b**, **2b'**, and **3b** and, in other cases, to the formation of particles of not enough quality to be characterized. The representative experiments were performed on the Ni derivative and later Pd and Pt nanoparticles were obtained using the conditions found in successful experiments of Ni.

(18) Eastoe, J.; Hollamby, M. J.; Hudson, L. *Adv. Colloid Interface Sci.* **2006**, *128/130*, 5–15.

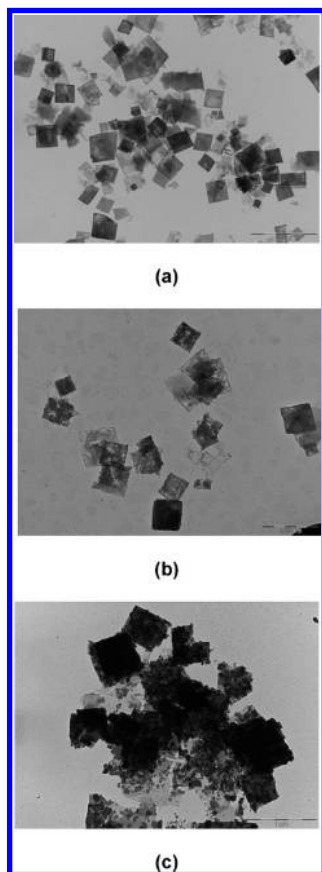


Figure 2. TEM images of the nanocrystals: **1a** (a), **2a** (b), and **3a** (c).

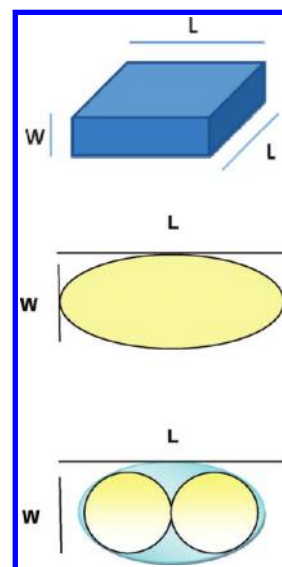
The most determinant factor influencing the growth of the $[\text{Fe}(\text{3-Fpy})_2\text{Ni}(\text{CN})_4]$ nanoparticles are the iron(II) and ligand concentrations ($[\text{Fe}^{\text{II}}]$, $[\text{3-Fpy}]$), the $[\text{PVP}]/[\text{Fe}^{\text{II}}]$ ratio, and the total volume used. In general, the size of the nanoparticles decreases as $[\text{Fe}^{\text{II}}]$ increases while other parameters including $[\text{PVP}]/[\text{Fe}^{\text{II}}]$ ratio are kept constant. This nanoparticle size reduction is even more remarkable when the concentration of 3-Fpy increases and the other parameters are kept constant. The effect of volume employed is also noticeable since it was found that the nanoparticle's dimension decreases when the volume is scaled up.

Particle Size Determination by TEM and SEM. Figure 2 shows the TEM images of nanocrystals **1a**, **2a**, and **3a** dispersed in ethanol and deposited on a TEM grid. The average particle size and distribution found are compiled in Table 2 and Supporting Information, Tables S2–S4. For statistical estimations of the dimensions L and W (Scheme 1) at least ~ 100 particles were evaluated for each sample using the ImageJ 1.38 software.¹⁹ Nanocrystals of **1a** and **2a** are well-defined; they consist of fairly mono-disperse nanocrystals with distinctive square faces of 444 ± 175 nm and 483 ± 128 nm side length, respectively. Preferred orientation of the crystals parallel to the grid surface made difficult their height determination by TEM and instead SEM images were used giving 45 ± 17 nm height estimation for **1a** and 30 ± 9 nm for **2a** (Figure 3).

Table 2. Average Particle Size and Distribution Found for the Nanocrystals and PVP Coated Nanoparticles of 1–3

	L (nm)	W (nm)
1a	444 ± 175	45 ± 17
1a*	400 ± 62	30 ± 6
2a	483 ± 128	30 ± 9
3a	481 ± 146	
1b	209 ± 54	138 ± 41
1b'	224 ± 41	100 ± 17
1c	127 ± 20	58 ± 10
1d	73 ± 13	33 ± 6
2b	292 ± 43	183 ± 32
2b'	221 ± 49	111 ± 27
3b	247 ± 43	181 ± 38

Scheme 1. Schematic Morphology of Nanocrystals **1a–3a** (top) and PVP Coated Nanoparticles of **1b–d** (Middle) and **2b–b'** (Bottom)



Although the quality of the nanocrystals of **3a** is lower than that of **1a–2a**, their morphology also corresponds to square crystals with average dimensions 481 ± 146 nm. However, SEM images of **3a** were not of sufficient quality to evaluate the width of the nanocrystals. Sample **1a*** was also characterized. It is made up of nanocrystals with average size similar to **1a** but interestingly with narrower distribution ($L = 400 \pm 62$ and $W = 30 \pm 6$ nm; Figure 3c, Supporting Information, Table S2).

Figure 4 gathers the TEM images of **1b**, **2b**, and **3b** while those corresponding to **1b'**, **1c**, **2b'**, and **3b** are illustrated in Supporting Information, Table S5. Table 2 and Supporting Information, Table S5 contain the corresponding experimental average size and distribution. Nanoparticles of **1b**, **1b'**, **1c**, and **1d** could be roughly described as cylinders with hemisphere endings. However, sample **2b** consists of nanoparticles of tightly “paired” spherical particles whereas they range from elongated to roughly spherical in sample **3b**.

Mössbauer Spectroscopy Characterization of the Bulk Materials, Nanocrystals, and Nanoparticles. The ^{57}Fe Mössbauer spectra of compounds **1–3** performed at two representative temperatures are shown in Supporting Information, Figure S4. The characteristic isomer shift

(19) Rasband, W. S. *ImageJ*; U. S. National Institutes of Health: Bethesda, MD, 1997–2007; <http://rsb.info.nih.gov/ij/>.

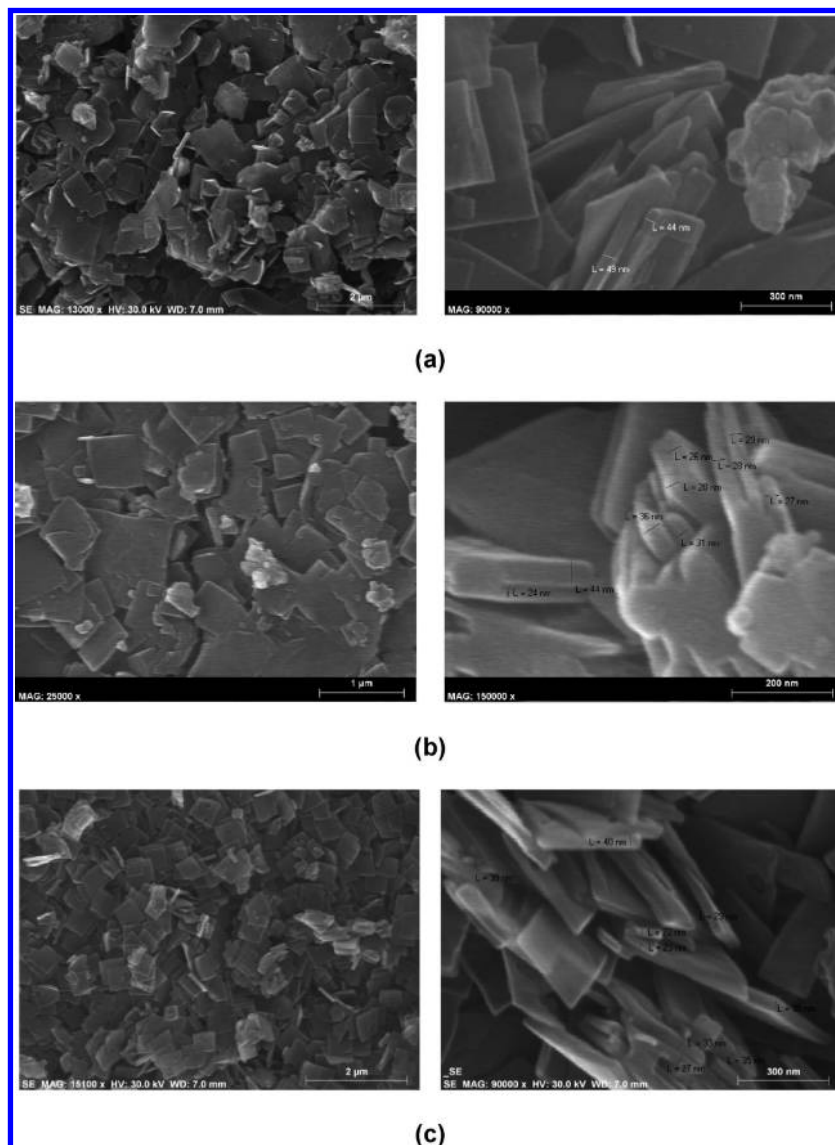


Figure 3. Scanning electronic microscopy (SEM) images of the nanocrystals **1a** (a), **2a** (b), and **1a*** (c).

(δ , relative to α -iron) and quadrupole splitting (ΔE_Q) parameters together with the percentage of population in HS and LS states deduced from the least-squares fit routine analysis of the spectra are given in detail for all compounds under study in Supporting Information Table S6. High-temperature Mössbauer spectra for **1–3** show only one doublet characterized by δ and ΔE_Q values in the ranges 1.06–1.07 mm s⁻¹ and 0.70–1.00 mm s⁻¹, respectively, which corresponds to the HS state. The intensity of this doublet decreases upon cooling down to 80 K at the expense of a new one featuring the LS doublet. The majority of the HS sites have transformed into the LS sites because of the spin crossover behavior. The population of the LS doublet is about 97% (**1**), 100% (**2**), and 97% (**3**).

High- and low-temperature ^{57}Fe Mössbauer spectra for **1a*** and **2a** are shown in Figure 5. High-temperature Mössbauer spectra show the occurrence of three different doublets, namely LS, HS(1), and HS(2) for both compounds. The LS doublet is characterized by δ and ΔE_Q values of 0.003–0.02 mm s $^{-1}$ and 0.20–0.22 mm s $^{-1}$,

respectively. The HS doublets show isomer shifts in the range 0.9–1.1 mm s^{−1} and quite different ΔE_Q values. For example, for **1a***, ΔE_Q is equal to 2.16 and 0.97 mm s^{−1} for the HS(1) and HS(2) doublets at 295 K, respectively, being their relative populations about 4% [HS(1)] and 86% [HS(2)]. The HS(2) doublet decreases in intensity upon cooling down to 4.2 K at the expense of the LS doublet ($\delta \sim 0.50$ mm s^{−1}, $\Delta E_Q \sim 0.23$ mm s^{−1}) whereas the population of the HS(1) doublet is practically temperature-independent. The slight increase observed in the relative population is most probably due to the increase of the Debye–Waller factor on lowering the temperature. At 4.2 K the relative population of the LS doublet is about 85%. Similar Mössbauer spectra have been observed for **2a**.

The Mössbauer parameters of **1** and **2** compare well with those found in **1a*** and **2a** for the HS(2) and LS sites. The relatively small ΔE_Q value of the HS(2) doublet stems from a large lattice contribution to the electric field gradient (EFG) arising from a distorted FeN_6 core with elongated D_{4h} symmetry which opposes the valence electron

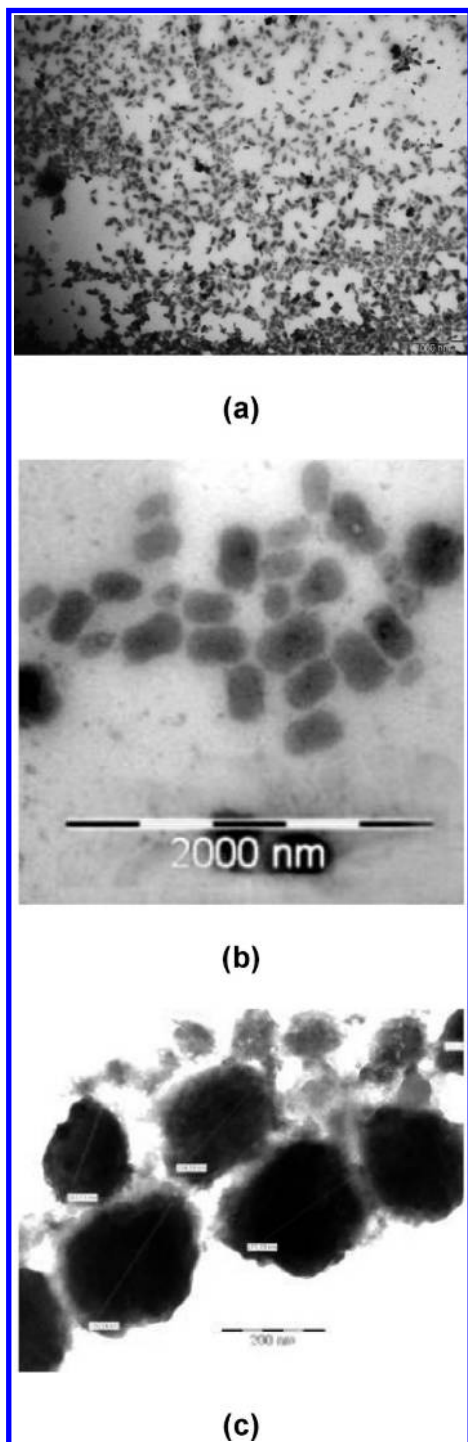


Figure 4. TEM images of the PVP coated nanoparticles: **1b** (a), **2b** (b), and **3b** (c).

contribution to the EFG. The HS(1) doublet characterized by a larger ΔE_Q is ascribed to the Fe(II) ions located at the nanocrystals edge as they must display coordinative “defects”, that is, coordinative unsaturation or coordinated terminal water molecules and, consequently, cannot exhibit SCO. This effect should be more prominent for small particles since they present a higher surface area. Taking into account the average size of **1a*** and **2a** nanocrystals ($400 \times 400 \times 30$ nm; $480 \times 480 \times 30$ nm) and the dimensions of the unit cell of **2** (isostructural to **1**) ($a \approx 15.5$ Å and $b \approx c \approx 7.3$ Å), a rough estimate of

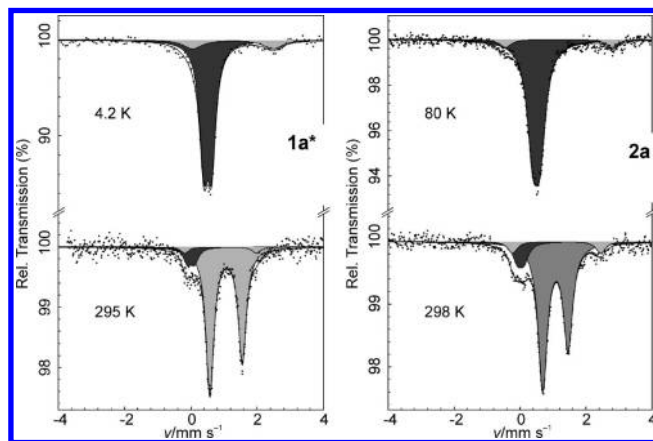


Figure 5. Mössbauer spectra of nanocrystals **1a*** and **2a** at different temperatures (dark gray corresponds to LS, gray and light gray to HS states).

possible incomplete coordination $\text{FeN}_x(\text{OH}_2)_y$ ($x + y = 6$) sites lying at the surface of the nanocrystals gives about 11% residual HS centers for **1a*** and **2a**. The calculated population of HS sites corresponds well to the experimental observation for the site HS(1), namely, 15% and 8% for **1a*** and **2a**, respectively. The presence of intrinsic defects in the crystal may additionally be a source of HS and/or LS residual fractions at low and/or high temperature, respectively. Indeed, it could account for 10% of residual LS species trapped at room temperature in **1a*** and **2a**.

Representative Mössbauer spectra of **1b–3b** are shown in Figure 6 while the spectra of **1c** and **1d** are depicted in Supporting Information, Figure S5. These spectra were deconvoluted in three doublets, namely, LS, HS(1), and HS(2). The HS sites are characterized by δ values in the $1.06\text{--}1.2$ mm s $^{-1}$ range and quite different ΔE_Q values (280/295 K: $2.40\text{--}2.62$ and $0.74\text{--}0.99$ mm s $^{-1}$; 100/70 K: $2.94\text{--}3.31$ and $1.47\text{--}2.35$ mms $^{-1}$, for the HS(1) and HS(2) doublets, respectively).

At 280 K, the relative population of HS(1) is 8% (**1b**), 11% (**1c**), 21% (**1d**), 17% (**2b**), 24% (**3b**) while it is about 64% (**1b**), 60% (**1c**), 53% (**1d**), 53% (**2b**), and 42% (**3b**) for HS(2). The population of the LS doublet is surprisingly large at this temperature being in the order of 28% (**1b**), 30% (**1c**), 34% (**1d**), 29% (**2b**), and 46% (**3b**) ($\delta \sim 0.2\text{--}0.4$ mm s $^{-1}$, $\Delta E_Q \sim 0.2\text{--}0.6$ mm s $^{-1}$). The intensity of the LS doublet increases at low temperature at the expenses of the HS(2) doublet whereas the population of the HS(1) doublet is practically temperature-independent. However, the majority of HS(2) sites do not transform into the LS sites in contrast to what was observed for the nanocrystals **1a–3a**. At 100 K, the population of the LS doublet is about 70% (**1b**), 69% (**1c**), 60% (**1d**), 64% (**2b**), 62% (**3b**) reflecting that the number of molecules in the high spin state is considerably large at this temperature, being around 30% for all nanoparticles under study. It should be noted that for compound **1c** it was necessary to introduce an additional HS doublet, at low temperature, to get a reasonable fit. This HS(3) site is also assigned to the Fe(II) atoms on the surface of the nanoparticle.

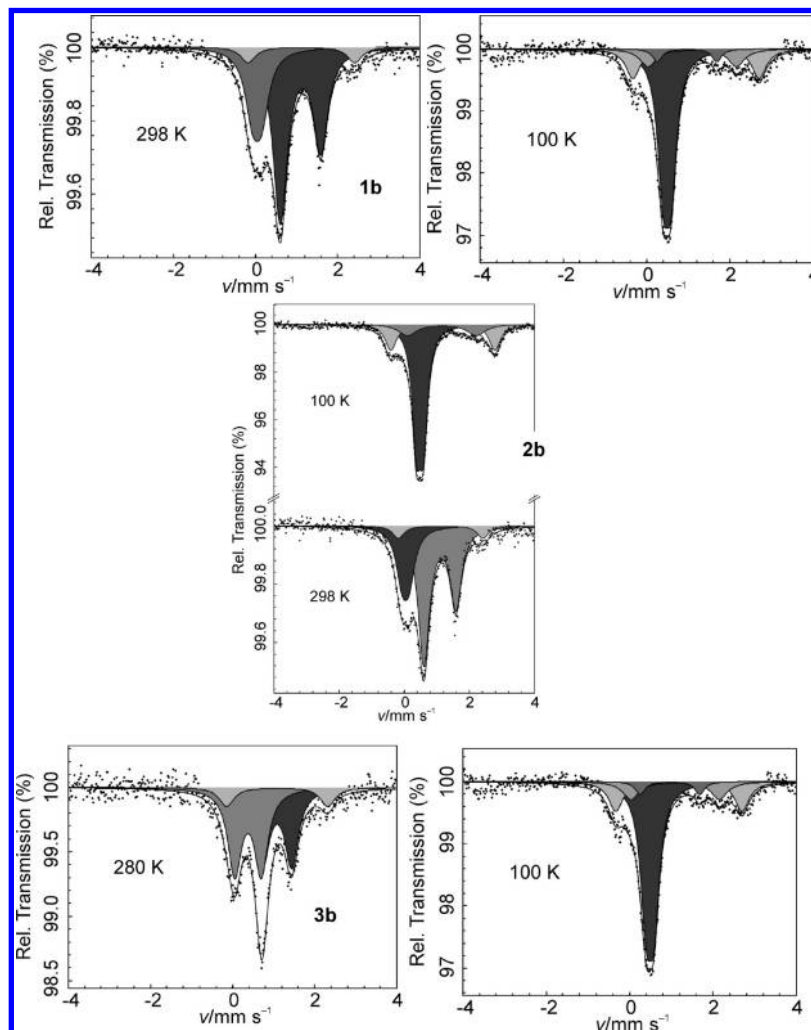


Figure 6. Mössbauer spectra of the PVP coated nanoparticles **1b** (a), **2b** (b), and **3b** (c) measured at 280 and 100 K (dark gray corresponds to LS, gray and light gray to HS states).

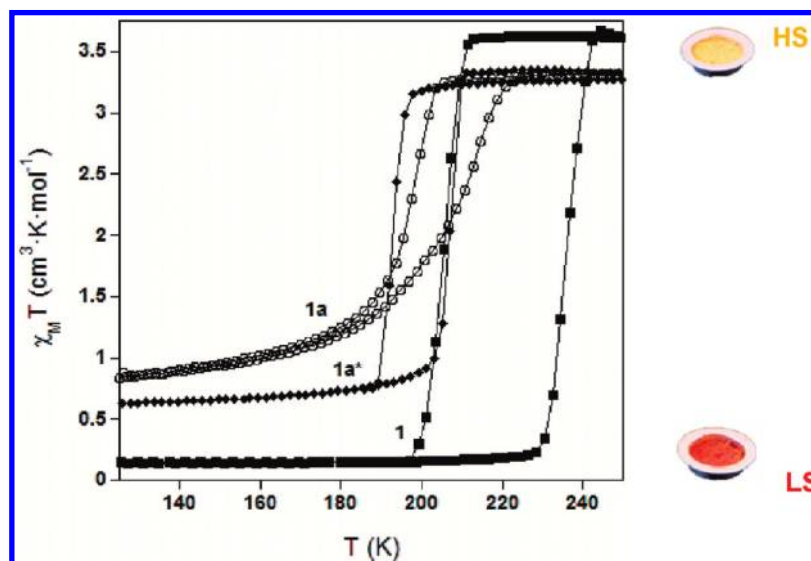


Figure 7. $\chi_M T$ versus T dependences for **1**, **1a**, and **1a*** recorded in 2–350 K temperature interval at the rate of 2 K/min in the cooling and warming modes (red color stands for LS state and yellow for HS state).

The Mössbauer spectroscopy has evidenced the different HS and LS sites present in the PVP coated nanoparticles **1b**, **2b**, **3b**, **1c**, and **1d** at high and low temperature.

This particular situation is the result of the polymer coating which creates different “chemical pressure” in the nanoparticles leading to different crystal field strength

at the iron sites. Therefore, only a fraction of the Fe(II) HS sites undergo spin transition whereas the rest remain in the HS or LS states.

Magnetic Properties of 1a–1d, 2a, 2b, 3a, and 3b. The thermal dependence of $\chi_M T$ for **1a**, **1a***, and the bulk compound **1** (χ_M stands for the molar magnetic susceptibility and T for temperature), is shown in Figure 7. The spin transition of the nanostructured compounds **1–3** is accompanied by pronounced color change (LS (red) and HS (yellow)). At 300 K, $\chi_M T$ is equal to 3.62, 3.36, and 3.36 $\text{cm}^3 \text{K mol}^{-1}$ for **1**, **1a**, and **1a***, respectively. The $\chi_M T$ value is lower for the nanocrystals than for the bulk compound because of the presence of a LS fraction at this temperature evidenced by the Mössbauer spectra of **1a***. On lowering the temperature, **1a** undergoes a first order spin transition ($T_c^\downarrow = 197 \text{ K}$ and $T_c^\uparrow = 207 \text{ K}$, where T_c is the critical temperature of the spin transition regarded as a first order phase transition), with the characteristic critical temperatures shifted down compared to similar transition in **1** ($T_c^\downarrow = 204 \text{ K}$ and $T_c^\uparrow = 234 \text{ K}$). Below T_c^\downarrow the magnetic susceptibilities are practically temperature independent. At 80 K, the $\chi_M T$ values of 0.12 $\text{cm}^3 \text{K mol}^{-1}$ (**1**) and 0.60 $\text{cm}^3 \text{K mol}^{-1}$ (**1a**) point out that a small residual HS fraction present at low temperature, which agree with the Mössbauer spectra.

The cooperativity associated with the spin crossover process diminishes as the particle size decreases. This is clearly reflected, for instance, in the change of the thermal hysteresis width from 30 to 10 K when moving from **1** to **1a**. Furthermore, **1a** does not exhibit a well-defined square shaped hysteresis loop as observed for **1**, denoting the occurrence of relatively large distribution of particle sizes. In contrast, the sample **1a*** displays smaller distribution of nanocrystal size and, as expected, exhibits a symmetric hysteresis loop at T_c 's similar to **1a** ($T_c^\downarrow = 192 \text{ K}$ and $T_c^\uparrow = 205 \text{ K}$) (Figure 7).

The thermal dependences of the HS molar fraction (γ_{HS}) for **1**, **1a***, and **1b–1d** derived from the magnetic susceptibility curves are depicted in Figure 8. The γ_{HS} value at low and high temperatures was fixed by the population of each spin state given by the Mössbauer spectra. For **1b–1d** the γ_{HS} at 293 K is around 0.7. All samples contain considerably high LS fractions in the high temperature region consistently with the Mössbauer investigations. The γ_{HS} values are practically temperature independent down to 200 K, decreasing upon further cooling as a consequence of a second order continuous spin state transition reaching a plateau centered at around $\gamma_{\text{HS}} = 0.3$ in the temperature range of 120–50 K. The Mössbauer parameters suggest that the HS fraction at this temperature corresponds to the Fe(II) ions located in the surface of the particles. The characteristic temperatures ($T_{1/2}$) at which $\gamma_{\text{HS}} = 0.5$ are 180 K (**1b**), 186 K (**1c**), and 176 K (**1d**). The further decrease of γ_{HS} below 50 K is essentially ascribed to zero field splitting of the Fe(II) ions remaining in the HS state at low temperature. The temperature dependence of γ_{HS} in warming and cooling modes coincide for **1b–1d**.

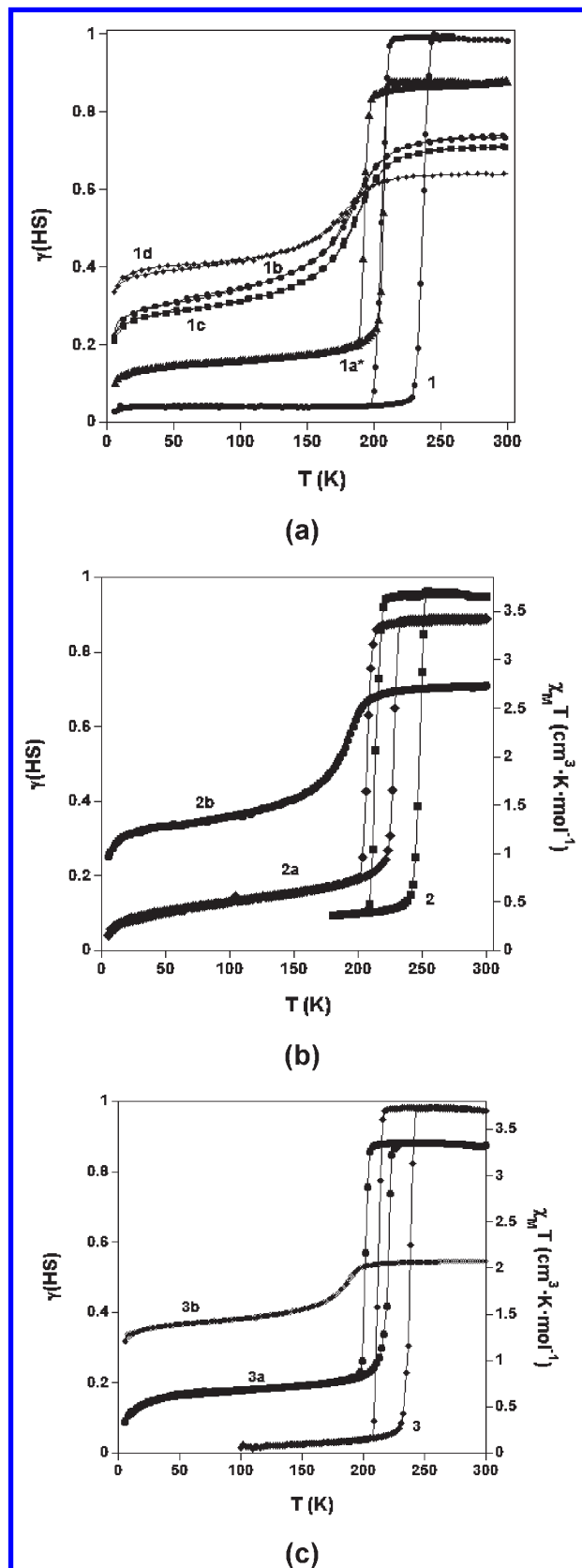


Figure 8. (a) Thermal dependence of the HS molar fraction (γ_{HS}) for **1**, **1a***, and **1b–1d** derived from the magnetic susceptibility curves recorded in the 2–350 K temperature interval at the rate of 2 K/min in the cooling and warming modes. $\chi_M T$ versus T and γ_{HS} versus T graphs for **2**, **2a**, **3**, **3a** and **2b** and **3b** (b) and (c).

The magnetic properties of **2a** and **3a** are illustrated in Figure 8. The $\chi_M T$ values found at 300 K are 3.67 (**2**), 3.41

(**2a**), 3.71 (**3**), 3.35 (**3a**) $\text{cm}^3 \text{K mol}^{-1}$ and are in accordance with the spin state populations given by the Mössbauer spectra. The magnetic susceptibilities remain practically temperature independent until the vicinity of T_c where they abruptly decrease within a few kelvins. The first order spin transitions take place at $T_c^\dagger = 211 \text{ K}$ (**2**), 205 K (**2a**), 211 K (**3**), 200 K (**3a**). In the low temperature region the $\chi_M T$ values are 0.09 (**2**) and 0.015 K (**3**) $\text{cm}^3 \text{K mol}^{-1}$, denoting that all iron(II) atoms have adopted the LS state in the case of the bulk compounds. For the nanocrystals, the $\chi_M T$ value is higher, about 0.5–1.0 $\text{cm}^3 \text{K mol}^{-1}$, and is in agreement with the HS population evidenced by the Mössbauer spectra at low temperature. In the warming mode the characteristic temperature is $T_c^\dagger = 246 \text{ K}$ (**2**), 225 K (**2a**), 237 K (**3**), and 219 K (**3a**), being the width of the hysteresis cycles of 35 K (**2**), 20 K (**2a**), 26 K (**3**) and 19 K (**3a**). It is remarkable that the shift of T_c to lower temperature occurs together with the reduction of the thermal hysteresis loop observed for **2a** and **3a**. Also, it is worth noting the square-shape of the hysteresis cycles, which reflect the relatively small size distribution found.

The γ_{HS} versus T dependences for the PVP-coated nanoparticle samples of **2b** and **3b** are shown in Figure 8. γ_{HS} remains practically constant in the range of 300–200 K with values of about 0.7 (**2b**) and 0.5 (**3b**). Cooling under 200 K leads to progressive decrease of γ_{HS} because of the occurrence of a second order spin transition, which takes place at $T_{1/2} = 190 \text{ K}$ (**2b**) and 185 K (**3b**). The transition is not complete, as also evidenced by Mössbauer spectroscopy. γ_{HS} values below $T_{1/2}$ are about 0.3 for **2b** and **3b**, and practically temperature independent down to 50 K. Because of the zero field splitting of the $S = 2$ spin state of Fe(II) ions and/or intermolecular antiferromagnetic interactions γ_{HS} slightly decreases below 50 K. On warming, the temperature dependence of γ_{HS} matches that of the cooling mode reflecting the complete reversibility of the spin transition process.

Discussion

The characteristic temperatures of the spin transition versus particle size for $[\text{Fe}(\text{3-Fpy})_2\text{Ni}(\text{CN})_4]$ (**1** series) are depicted in Figure 9. $T_c^{\text{av}} = (T_c^\dagger + T_c^\ddagger)/2$ is given for the bulk material and nanocrystals whereas $T_{1/2}$ is considered for nanoparticles. In this correlation we have arbitrarily assigned a size of 1000 nm to the crystallites of the bulk material. The dependence of the characteristic temperature on the particle size follows a logarithmic behavior for **1**, which is in accordance with the results found in similar studies of the 3D polymer $[\text{Fe}(\text{pz})\text{Pt}(\text{CN})_4]$.^{9,10} For derivatives **2** and **3**, despite that there is no information for particles smaller than $200 \times 100 \text{ nm}$, the trend is similar.

The logarithmic form indicates the evolution of the effective crystal field strength “felt” by the iron(II) centers with the particle size, which also affects the cooperativity. Apparently, diminution of the particle size produces a decrease of the “chemical pressure” on the spin transition centers, thereby decreasing the transition temperature. This functional form with respect to the particle size has

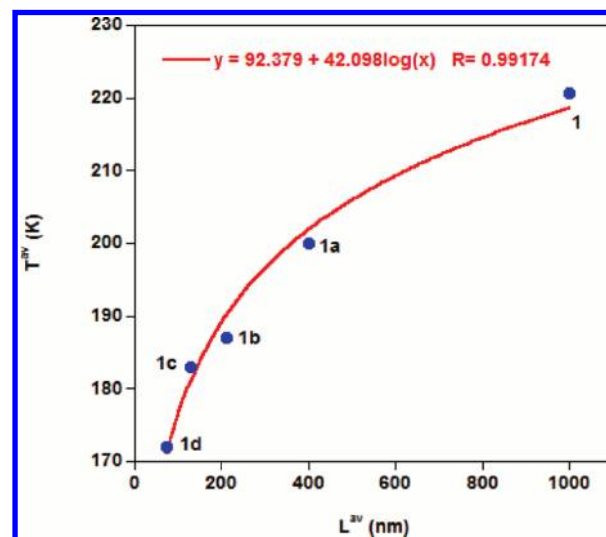


Figure 9. Characteristic temperatures of the spin transition versus particle size for $[\text{Fe}(\text{3-Fpy})_2\text{Ni}(\text{CN})_4]$ materials (characteristic temperatures are given as $T_c^{\text{av}} = (T_c^\dagger + T_c^\ddagger)/2$ for the bulk compound, **1**, and nanocrystals, **1a**, and as $T_{1/2}$ for the PVP coated nanoparticles, **1b–d**).

also been observed, for several physical properties, in nanocrystals of CdS, ZnS, CdSe, or NaCl.²⁰

The dependence of the hysteresis width on particle size for **1–3** and $[\text{Fe}(\text{pz})\text{Pt}(\text{CN})_4]$ corresponds well to the behavior predicted by Monte Carlo simulations for cubic or spherical spin crossover nanoparticles.¹⁶ However, these simulations predict a much weaker (almost negligible) dependence of T_c on particle size than the observed one for **1–3** and $[\text{Fe}(\text{pz})\text{Pt}(\text{CN})_4]$. This discrepancy may reflect the oversimplified nature of the model employed, in which only short-range elastic interactions²¹ have been taken into account. Indeed, significant influence of long-range interactions on the cooperativity of the SCO process was inferred from infrared and Raman studies of the $[\text{Fe}(\text{pz})\text{M}(\text{CN})_4]$ and $[\text{Fe}(\text{pyridine})\text{M}(\text{CN})_4]$ series.^{15b,c}

It is worthwhile to note that the observed correlation between SCO (critical temperature, hysteresis width, and residual HS/LS state sites) and size of the nanocrystals/nanoparticles is reminiscent of that derived from the isomorphous solid solutions studies of $[\text{Fe}_{1-x}\text{M}^{\text{II}}_x(\text{pz})\text{Pt}(\text{CN})_4]$ ($0 \leq x \leq 1$, $\text{M}^{\text{II}} = \text{Ni}, \text{Co}$).^{15b} Dilution with non-SCO Ni(II) or Co(II) ions reduces progressively the size of the SCO domains thereby decreasing cooperativity, shifting T_c downward, and converting the first order spin transition into a second order continuous one, accompanied with narrowing of the hysteresis loop width until its disappearance at $x = 0.60$.

The nanostructuring of polymers **1–3** and $[\text{Fe}(\text{pz})\text{Pt}(\text{CN})_4]$ has provided better insight into the correlation between cooperativity and dimensionality of the polymer. Despite SCO materials based on the 2D polymers **1–3** and the 3D one $[\text{Fe}(\text{pz})\text{Pt}(\text{CN})_4]$ feature about 25 K hysteresis loops of similar width and similar cooperative “efficiency” of the networks sustaining

(20) (a) Alivisatos, A. P. *J. Phys. Chem.* **1996**, *100*, 13226. (b) Baker, M. D.; Baker, A. D. *J. Chem. Educ.* **2010**, *87*, 280. (c) Breaux, G. A.; Benirschke, R. C.; Jarrold, M. F. *J. Chem. Phys.* **2004**, *121*, 6502.

a first-order SCO process, it might be suggested that the actual minimum spin crossover domain is notably different. A quasi complete first order spin transition is observed for nanocrystals of $[\text{Fe}(\text{pz})\text{Pt}(\text{CN})_4]$ with about $50 \times 50 \times 20$ nm size⁹ while for **1a–3a** this behavior is observed for nanocrystals of about $400 \times 400 \times 30$ nm. The nanoparticles **1b–3b**, sized around 200×100 , 100×60 , and 70×30 nm, undergo incomplete second order spin transition whereas first order transition is still observable for the nanocrystals¹⁰ of $[\text{Fe}(\text{pz})\text{Pt}(\text{CN})_4]$ with maximum dimensions not exceeding 15 or 4 nm (the transiting fraction of Fe(II) sites is also modest, but the character of the transition including the presence of hysteresis with a few kelvin width is better retained). This experimental fact clearly demonstrates that the 3D polymer $[\text{Fe}(\text{pz})\text{Pt}(\text{CN})_4]$ enables better cooperativity of the spin-transition process as was previously anticipated.¹⁶

The puzzling results reported for 1D triazole based SCO nanoparticles makes difficult any comparison with those results found for 2D and 3D Hofmann Clathrate analogue SCO nanocrystals/nanoparticles.

Conclusion

Here we have shown that nanocrystals and nanoparticles of $[\text{Fe}(\text{3Fpy})_2\text{M}(\text{CN})_4]$ 2D SCO coordination polymers can be obtained by applying the reverse micelle technique or using a coating polymer such as PVP, respectively. The SCO properties have been evidenced to be drastically influenced by the dimensions of the crystal/particle. Square like nanocrystals of Ni, Pt, and Pd derivatives with dimensions $400 \times 400 \times 30$ nm undergo a first order spin transition. Independently from its morphology, nanoparticles of average size 200×100 , 100×60 , and 70×30 nm exhibit an incomplete and continuous second order spin transition.

Aside from fundamental importance of the new experimental data on gathering deeper insight into the correlation between particle size and SCO parameters in Fe(II) coordination polymers, the developed nanostructured SCO materials could be viewed as potential prototypes for technological applications near room temperature, that is, sensors and thermally switchable memories.

Acknowledgment. Financial support is acknowledged from the Spanish Ministerio de Educación y Ciencia (MEC) (CTQ 2007-64727-FEDER), from the Generalitat Valenciana (GVPRE/2008/150 and ACOMP09/326), and from the European Network of excellence MAGMANET (Contract: NMP3-CT-2005-515767-2). We also acknowledge the financial help from the Deutsche Forschungsgemeinschaft (Priority Program 1137 “Molecular Magnetism”). A.B.G. thanks the Spanish MEC and the FGUV for a research contract (Programa I3). We thank Dr. M. Seredyuk for helpful discussions.

Supporting Information Available: IR spectra of bulk compounds **1–3** and nanocrystals **1a–3a** at 293 K. Comparative IR spectra of PVP covered nanoparticles **1b**, the polymer and the bulk material at 293 K. TGA analyses of bulk compounds **1–3** and nanocrystals **1a–3a**. Series of experiments performed in the synthesis of nanocrystals of compounds **1–3** applying the reverse micelle method and using the coating polymer PVP. Images used for particle size determination and the resultant statistics for all the newly synthesized materials. Mössbauer spectra of **1–3**, **1c**, and **1d** measured at two different temperatures; the characteristic isomer shift (δ , relative to α -iron) and quadrupole splitting (ΔE_Q) parameters together with the percentage of population in HS and LS states deduced from the least-squares fit routine analysis of the spectra for **1–3** and the nanostructured compounds **1a***, **2a**, **1b–1d**, **2b**, and **3b**. Estimation of the percentage of Fe(II) sites at the surface of the nanocrystals for **1a*** and **2a**. Powder X-ray diffraction patterns of **1–3** (calculated), **1a–3a** and **3b** (experimental) at 293 K. This material is available free of charge via the Internet at <http://pubs.acs.org>.

(21) Spiering, H. *Top. Curr. Chem.* **2004**, 235, 171.